Results in Materials 14 (2022) 100283

Contents lists available at ScienceDirect

Results in Materials

journal homepage: www.sciencedirect.com/journal/results-in-materials

Rapid multi-property assessment of compositionally modulated Fe-Co-Ni thin film material libraries

Shakti P. Padhy [a,1], Z. Tsakadze [a,1], V. Chaudhary [a,*], G.J. Lim [b], X. Tan [a], Wen Siang Lew [b], R.V. Ramanujan [a,*]

[a] School of Materials Science and Engineering, Nanyang Technological University, 639798, Singapore
[b] School of Physical and Mathematical Sciences, Nanyang Technological University, 637371, Singapore

ARTICLE INFO

Keywords:
Combinatorial method
Thin film materials libraries
High-throughput screening
Multiple property assessment

ABSTRACT

Next-generation high frequency, high power density, and high operating temperature electrical machines require superior materials which possess an attractive combination of structural as well as functional properties. Development of such new materials by conventional methods is very slow, expensive, and restricted to a few compositions. Hence, we addressed this challenge by the accelerated assessment of multiple properties of a range of Fe-Co-Ni based material compositions. We utilized the magnetron co-sputtering method to prepare compositionally modulated ternary Fe-Co-Ni thin film alloy (TFA) libraries. The structural, electrical, magnetic, and mechanical properties of these libraries were assessed. The structure and properties were found to vary over a wide range with composition and thin film processing parameters. The Fe-Co-Ni TFA library prepared at a substrate temperature of 500 °C exhibited a good combination of multiple properties. The specific alloy composition $Ni_{54.9}Co_{33.1}Fe_{12}$ was found to possess an attractive blend of properties. Thus, a rapid property assessment of TFA libraries of a wide range of compositions and processing conditions was successfully used to identify a novel specific composition and processing protocol which exhibited an attractive mix of properties.

1. Introduction

Materials play a vital role in electromagnetic and energy conversion devices such as rotating electric machines, electrical transformers, electromagnetic shielding components, sensors, actuators, magnetic-MEMS, and magnetic recording media [1–6]. Such systems are used in a very broad range of applications and industry verticals, e.g., electric vehicles. There is an urgent demand for superior materials in next generation technological applications, e.g., high frequency, high power density, high magneto-mechanical response, high operating temperature rotating electrical machines. Multiple properties, such as mechanical, electrical, and magnetic properties need to be satisfied for such applications. The use of superior materials will improve service life, performance and reduce greenhouse gas emissions and electricity consumption. Electric motors account for a major percentage of electricity consumption globally; improving their efficiency by just 1% would reduce global power consumption by 94.5 TW-hours and the carbon dioxide footprint by 60 million metric tons [7].

Currently, there is no single alloy composition which possesses the multi-property set needed to develop next-generation systems. For example, a given alloy composition may have good magnetic properties but display poor resistivity or inferior mechanical properties. The alloy composition $Fe_{70}Co_{30}$ exhibits the highest saturation magnetization (M_s) [8,9], on the other hand, it is Ni–Fe alloys which exhibit high permeability and low coercivity (H_c) [8,10]. Silicon steel (Fe–Si alloy) is a different alloy family which exhibits high M_s and relatively high electrical resistivity (ρ) compared to binary Fe–Co and Ni–Fe alloys [11]. Since a single known alloy composition does not usually possess the required set, it is necessary to deploy new techniques to identify novel alloy compositions possessing an appropriate set of property values.

M_s, electrical resistivity, mechanical properties, Curie temperature (T_c) and H_c are some typical properties needed for rotating electrical machines [2–4,12–14]. For example, a magnetic high-entropy alloy (HEA) based on the multi-component Fe-Co-Ni–Ta–Al alloy system [15] could be processed to display better mechanical properties, although accompanied by a small increase in coercivity. This set of change in

* Corresponding authors
E-mail addresses: varun004@e.ntu.edu.sg (V. Chaudhary), ramanujan@ntu.edu.sg, ramanujan@ntu.edu.sg (R.V. Ramanujan).
[1] Authors contributed equally.

https://doi.org/10.1016/j.rinma.2022.100283
Received 12 April 2022; Accepted 8 May 2022
Available online 14 May 2022

properties was attributed to the formation of coherent and ordered nanoprecipitates in the HEA matrix, these precipitates impeded dislocation motion but did not significantly hinder domain walls. Thus, exploration of a wide composition space, along with a range of processing parameters, holds the key to identifying novel material compositions possessing an attractive property set.

Developing such new materials through the conventional methods of synthesis and characterization is tedious, expensive, and most

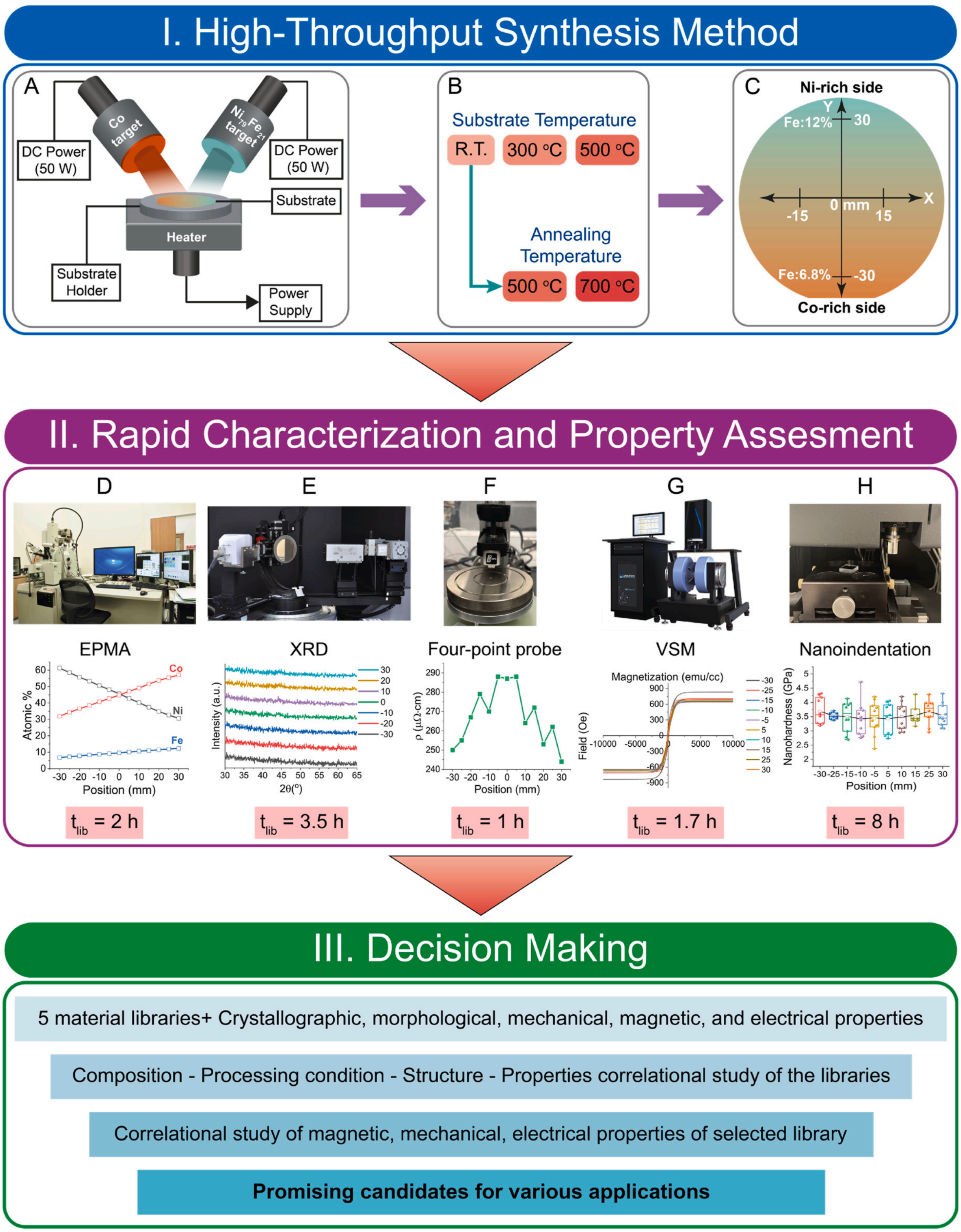

Fig. 1. Overview of synthesis, property assessment, and decision strategies used for compositionally graded Fe-Co-Ni thin film alloy (TFA) libraries. (A) Schematic of magnetron co-sputtering deposition technique. (B) Variation of processing conditions via substrate temperature and annealing temperature for 5 TFA libraries. (C). Schematic of a TFA library and notation used for characterization and property assessment. The techniques (D) Electron Probe Microanalyzer (EPMA), (E) X-ray Diffraction (XRD), (F) Four-point probe, (D) Vibrating Sample Magnetometer (VSM), and (E) Nanoindentation used for rapid assessment of composition, crystallographic structure, electrical, magnetic, and mechanical properties respectively. t_{lib} represents the time taken for characterization and property assessment for each TFA library.

importantly, very severely limits the possibility of exploring the vast composition and processing space [16,17]. Hence, high throughput methods of synthesis and characterization are essential to accelerate the exploration of new materials [2,4,9,13,14,16,18–26]. High throughput thin film methods have been deployed to discover new materials, e.g., $Fe_{73.2}Co_{24.2}Ir_{2.6}$ and $Fe_{84}Co_{12}Pt_4$ with a magnetic moment higher than $Fe_{70}Co_{30}$ [9], $Fe_{51}Co_{41}V_8$ as a novel permanent material [14], and 2 at% Ga-ZnO transparent conducting oxide for organic light emitting diodes [16].

$(Fe,Co)_3Nb$ precipitates, formed in a Fe–Co matrix in a Fe–Co–Nb thin film library exhibited both hard and soft magnetic behaviour [27]. A Ni–Ti–Cu (Ti = 65–67%, Cu = 0–4%) thermoelastic shape memory alloy composition exhibiting a small thermal hysteresis width [28] was identified by a combinatorial synthesis and high throughput property characterization method. Novel shape memory alloy compositions ($Ni_{29.1}Ti_{64.3}Co_{6.6}$ and $Ni_{32.8}Ti_{61.3}Co_{5.9}$) with near zero thermal hysteresis [29], and a $Ni_{40}Cr_{60}$ alloy compositions for corrosion resistant applications [30] have been identified using accelerated methodology.

Iwasaki et al. [9] used machine learning and *ab-initio* calculations to explore the vast multicomponent Fe-Co-Ni–Ru–Rh–Pd–Ir–Pt alloy system and predicted a specific composition, $Fe_{82}Co_{13}Ir_4Pt_1$, with high magnetic moment. Combinatorial studies on Fe–Co–V, Fe–Ni, Fe-Co-Ni, Al–Co–Ni, etc. thin film systems have been performed using high throughput characterization techniques [14,19,24,31,32] Two amorphous phase regions (near the binary compositions $Fe_{50}Co_{50}$ and $Fe_{50}Ni_{50}$) were identified in the ternary Fe-Co-Ni alloy system [32].

The novelty of this work is the rapid assessment of structural, magnetic, electrical, and mechanical properties of ternary alloy thin films. There has been no detailed study of ternary Fe-Co-Ni alloys, although the counterpart binary alloys and single elements have been examined [4]. The vast ternary composition-structure-property space provides significant scope to discover new alloy compositions and processing conditions with an useful combination of properties.

Hence, we present the combinatorial assessment of compositionally modulated Fe-Co-Ni thin film alloy (TFA) libraries prepared using a magnetron co-sputtering technique. The development of structural, electrical, magnetic, mechanical and wear resistance property libraries as a function of composition and processing parameters is described. The optimum process parameters and compositions with balanced properties are identified. Fig. 1 shows the schematic of the high-throughput synthesis and characterization methodology, followed by the data analysis strategy used to identify promising compositions.

2. Experimental methodology

Compositionally graded Fe-Co-Ni films were synthesized by DC magnetron co-sputtering (Fig. 1(a)) using $Ni_{79}Fe_{21}$ (purity ≥99.95%) and Co (purity ≥99.95%) targets (Kurt J. Lesker Company, Jefferson Hill, PA, USA). A power supply of 50 W was used for both targets. The experiments were performed in argon atmosphere for a constant deposition time. The sputtering chamber was evacuated to 6.67×10^{-6} Pa base pressure, deposition was then carried out at a working pressure of 0.67 Pa in flowing argon at a flow rate of 20 standard cubic centimetre per minute (sccm).

Two experimental protocols were followed (Fig. 1(b)):

(i) Fe-Co-Ni TFA libraries were deposited on SiO_2/Si substrates at three different substrate temperatures (T_s): room temperature (**ML_{RT}**), 300 °C (**ML_{300}**), and 500 °C (**ML_{500}**); and
(ii) Fe-Co-Ni TFA libraries were deposited at RT and annealed at two different temperatures (T_a): 500 °C (**$ML_{500\text{-}SC}$**) and 700 °C (**$ML_{700\text{-}SC}$**) for 2 h in the sputtering chamber (SC) at a pressure of 6.7×10^{-6} Pa.

The chemical compositions of the films were determined using a JEOL JXA-8530F Electron Probe Microanalyzer (EPMA). High-throughput X-ray diffraction (XRD) analysis of the compositionally graded films was carried out using a Bruker D8 Discover diffractometer using Cu Kα radiation. The operating voltage and current were 40.0 kV and 40.0 mA, respectively. The morphology was examined by a Field Emission Scanning Electron Microscope (FESEM) (JEOL JSM-7800F Prime). The thickness profile was measured using an Alpha-Step D500 Stylus Profilometer (KLA Tencor, Milpitas, CA, USA) on a patterned sample. This sample was prepared using the photoresist, AZ 5214 e, followed by baking at 100 °C for 5 min to dehydrate. The photoresist was lifted-off after co-sputtering by sonicating the wafer with acetone for 2 min, followed by isopropanol for 2 min.

A four-point probe tester (Keithlink) was used to determine the electrical resistivity of the films at different positions along x = 0 mm (Fig. 1(C)). The magnetic properties were measured by a Lakeshore 8604 vibrating sample magnetometer (VSM) for magnetic fields up to 10 kOe and 18 kOe for the in-plane (IP) and out-of-plane (OOP) arrangements, respectively. The samples for this measurement were cut at 10 different positions along the diameter of the wafer, i.e., along x = 0 mm (Fig. 1(C)). The hardness and elastic modulus of similarly cut samples were measured using a Nanoindenter G200 (KLA Tencor, Milpitas, CA, USA) instrument, equipped with a Berkovich tip using a depth control model for an indentation depth of 80 nm. An array of 10 points, with each point 10 μm apart, was used to measure each composition of the TFA library.

3. Results and discussion

3.1. Chemical composition analysis of the thin film alloy (TFA) libraries

Fig. 2(a) shows the composition profile of the TFA libraries (ML_{RT}, ML_{300}, and ML_{500}) along the diameter (x = 0 mm, Fig. 1(C)) synthesized at three substrate temperatures (room temperature (RT), 300 °C and 500 °C). The composition profile of the ML_{RT} TFA library is presented in section S1 of supplementary information. As expected, in the ML_{RT} TFA library, the cobalt content linearly decreased from the side of the film near the cobalt target during deposition to the opposite side of the film near the permalloy target, while the content of nickel and iron gradually increased. The same tendency of elemental distribution was also observed in the films deposited at higher substrate temperatures (ML_{300} and ML_{500}). The Co content was slightly higher in the ML_{500} film, while the Ni content was higher in the ML_{300} film. This effect can be attributed to the higher desorption rate of nickel adatoms as substrate temperature increases [33]. Fig. 2(b) shows the composition gradient of the three different TFA libraries: ML_{RT}, $ML_{500\text{-}SC}$, $ML_{700\text{-}SC}$. Annealing of these film libraries did not significantly change the composition gradient.

3.2. Thickness profile of the TFA library

Fig. 2(c) shows the 3D colour map of the thickness profile of the ML_{RT} TFA library. Fig. 2(d) shows the variation of thickness with distance along the diameter of the film, which corresponds to the thickness profile along x = 0. It can be observed that the thickness profile is quite symmetrical along x = 0. The slight differences can be attributed to the non-uniform thickness and height of the mask. The average thickness of the film is 817.7 nm. In Fig. 2(d), the sudden drop in thickness from −30 mm to −23 mm and from 30 mm to 26 mm can be attributed to the combined effect of higher deposition at the edges due to the shorter distance to the respective targets and mask shadowing at −23 mm and 26 mm. The thickness of the film measured at 30 mm was 916.5 nm and at −30 mm was 875.8 nm. Moreover, from-13 mm to 16 mm, the thickness of the film increased from 808.6 nm to 847.9 nm. These results indicate that the deposition rate of the $Ni_{79}Fe_{21}$ target is higher compared to that of the Co target. The deposition rates of $Ni_{79}Fe_{21}$ target and Co target were determined to be 0.045 nm/s and 0.0034 nm/s, respectively, which are in accordance with the thickness results.

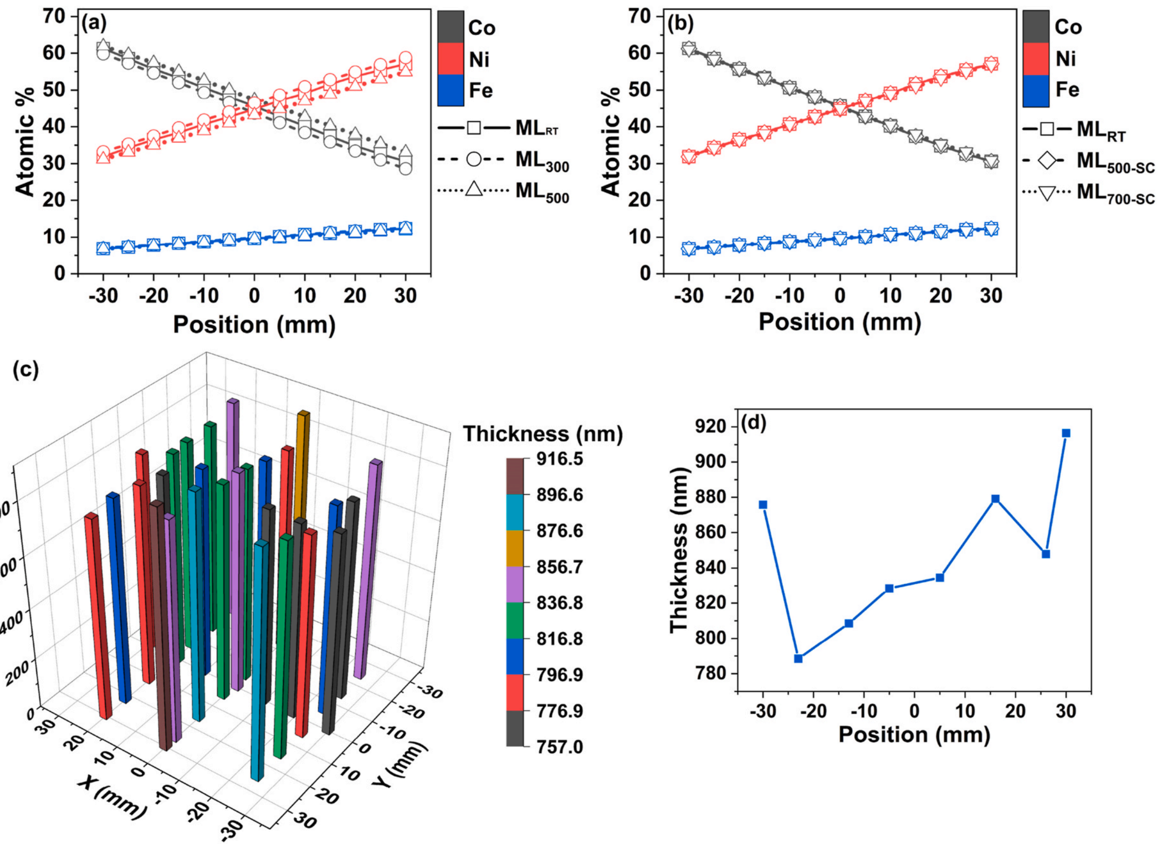

Fig. 2. Composition profile of TFA libraries (a) ML_{RT}, ML_{300}, and ML_{500} and (b) ML_{RT}, $ML_{500\text{-}SC}$, and $ML_{700\text{-}SC}$. (c) 3D colour map of thickness profile and (d) Thickness vs. position along x = 0 mm of TFA library ML_{RT}. (For interpretation of the references to colour in this figure legend, the reader is referred to the Web version of this article.)

3.3. Structural and phase analysis of the TFA libraries

Fig. 3(a)-(c) shows the XRD patterns of the TFA libraries ML_{RT}, ML_{300}, and ML_{500}, along x = 0 mm. The compositionally graded TFA library ML_{RT} was amorphous (Fig. 3(a)) due to the limited surface diffusion of adatoms [8], it falls under Zone 1 for the working pressure according to the structure zone model (SZM) [34]. When T_s was increased to 300 °C (Fig. 3(b)), adatom diffusion increased, leading to improved crystallinity. At this T_s and working pressure, ML_{300} falls under Zone 1. A single-phase face centred cubic structure (FCC) with a (111) texture was observed for all compositions.

T_s of 500 °C corresponds to higher T_s/T_m (substrate temperature/melting point of the deposited film material), referred to as Zone T in the SZM. At 500 °C, sputtered particles have higher energy, resulting in enhanced adatom mobility and diffusivity, giving rise to better crystallinity. The diffraction peaks grew sharper and peak broadening decreased (Fig. 3(c)). The intensity of the FCC diffraction peaks gradually reduced with an increase in nickel and iron content.

Fig. 3(d) and (e) shows the XRD patterns of the TFA libraries $ML_{500\text{-}SC}$, and $ML_{700\text{-}SC}$. For both the cases, XRD patterns revealed two small diffraction peaks, corresponding to the hexagonal closed packed structure (HCP) with (100) texture and FCC (111), at 2θ of 41.8° and 44.2°, respectively. As expected, the HCP phase is dominant on the Co-rich side and gradually decreased towards the Ni-rich side, eventually disappearing, corresponding to FCC phase formation. With an increase in annealing temperature, the crystallinity of the film increased; the diffraction peaks grew sharper, and the broadening of the peaks decreased. The volume fractions of the HCP and the FCC phases were determined at each scan position by Rietveld refinement and is presented in Table 1.

3.4. Film morphology

The SEM images of the Co-rich regions of ML_{RT} and ML_{300} (Fig. 4(a) and (b)) revealed the formation of surface void networks [35] which can be attributed to residual internal stress during the deposition process [36]. ML_{300} exhibited a higher surface void network density. For ML_{500} (Fig. 4(c)), no surface void network was observed, this film exhibited mostly a uniform morphology.

From Fig. 4(a), a maximum surface void network length (SVNL) and width (SVNW) of 665.9 nm and 37 nm, respectively was observed for ML_{RT}. From Fig. 4(b), a maximum SVNL of 1.365 μm and a maximum SVNW of 45 nm was observed for ML_{300}. The surface void networks in ML_{300} were wider and longer than the surface void networks in ML_{RT}. ML_{300} had a granular structure (average grain size = 98.6 nm) while ML_{500} (average grain size = 63.4 nm) and ML_{RT} (average grain size = 69 nm) had a particle-like structure. $ML_{500\text{-}SC}$ (Fig. 4(d)) exhibited more surface void networks compared to ML_{RT}. $ML_{700\text{-}SC}$ (Fig. 4(e)) showed equiaxed large size grains. After annealing, the films exhibited a larger grain size, which increased with annealing temperature. The average grain size of film ML_{RT} was measured to be 69 nm, which increased to 82 nm and 152.5 nm for the films $ML_{500\text{-}SC}$ and $ML_{700\text{-}SC}$, respectively. These results are summarized in Table 2.

3.5. Electrical resistivity of the TFA libraries

Fig. 5(a) shows the electrical resistivities (ρ) of all the compositionally graded TFA libraries, measured from the Co-rich side to the Ni-rich side. The ρ values of the film were larger with an increase in T_s from RT to 300 °C. The films prepared at 500 °C exhibited the lowest ρ values. The ρ values varied in the range from 244 μΩ·cm to 288 μΩ cm, from 314 μΩ·cm to 420 μΩ cm, and from 113 μΩ·cm to 163 μΩ cm for the TFA

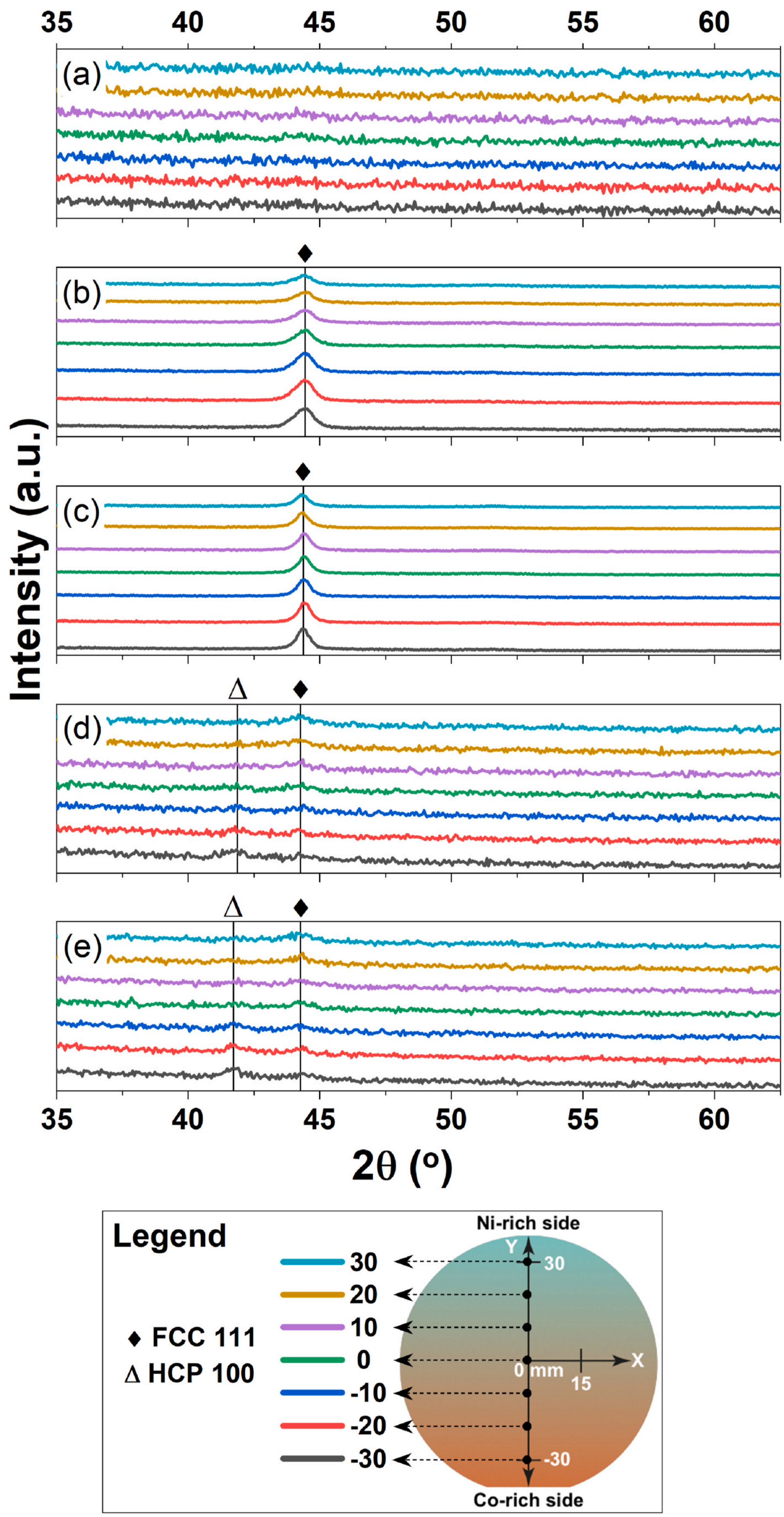

Fig. 3. XRD patterns of TFA libraries (c) ML_{RT}, (d) ML_{300}, (e) ML_{500}, (f) $ML_{500\text{-}SC}$, and (g) $ML_{700\text{-}SC}$.

Table 1
Volume fractions and ratio of HCP and FCC phases at each scan position of $ML_{500\text{-}SC}$, and $ML_{700\text{-}SC}$ TFA libraries.

Distance (mm)	$ML_{500\text{-}SC}$ film library			$ML_{700\text{-}SC}$ film library		
	HCP %	FCC %	HCP/FCC	HCP %	FCC %	HCP/FCC
−30	63.9	36.1	1.77	80.5	19.5	4.13
−20	58.7	41.3	1.42	58.9	41.1	1.43
−10	47.5	52.5	0.91	55.5	44.5	1.25
0	31.2	68.8	0.45	45.6	54.4	0.84
10	20.7	79.3	0.26	29.6	70.4	0.42
20	10.6	89.4	0.12	0	100	0
30	0	100	0	0	100	0

libraries ML_{RT}, ML_{300}, and ML_{500}, respectively. The crystallinity of the films increased as T_s increased from RT to 300 °C [37]. However, ρ increased although the crystallinity improved, and the grain size was larger. This effect is due to the formation of a higher surface void network density at $T_s = 300$ °C compared to RT, as discussed earlier. With a further increase of T_s to 500 °C, ρ reduced significantly due to the uniform film morphology. Annealing the TFA library ML_{RT} reduced the ρ for all the compositions as a result of the increase in grain size, which tends to lower ρ for metallic films [38,39].

For the TFA library $ML_{500\text{-}SC}$, the ρ varied in a small range from 178 to 185 μΩ cm for compositions varying from $Co_{61.3}Ni_{31.9}Fe_{6.8}$ to $Ni_{51.6}Co_{37.4}Fe_{11}$ and then decreased to the lowest value of 159 μΩ cm for $Ni_{57.1}Co_{30.6}Fe_{12.3}$. The ρ of the TFA library $ML_{700\text{-}SC}$ increased from 126 μΩ cm for $Co_{61.3}Ni_{33.2}Fe_{6.8}$, reaching a maximum of 137 μΩ cm for $Co_{48.1}Ni_{42.7}Fe_{9.2}$ and $Co_{45.6}Ni_{44.8}Fe_{9.6}$ and thereafter decreased to 118 μΩ cm for $Ni_{57.1}Co_{30.6}Fe_{12.3}$. In both the annealed TFA libraries, the highest ρ was observed near the centre of the film. This can be attributed to the dependence of ρ on the microstructure, interfacial boundaries, grain size, and texture in multi-phase alloys [40].

3.6. Magnetic properties of the film libraries

Fig. 5(b) and (c) shows the in-plane (applied magnetic field is parallel to the surface of the substrate) coercivity (H_c) and saturation magnetization (M_s) of the TFA libraries. With increasing Ni content, the in-plane H_c decreased from 117.8 to 59.8 Oe in ML_{RT}, from 155.1 to 56.9 Oe in ML_{300}, and from 95 to 64.5 Oe in ML_{500}. From ML_{RT} to ML_{300}, the in-plane H_c of the Co-rich compositions (from $Co_{61.3}Ni_{33.2}Fe_{6.8}$ to $Co_{48.1}Ni_{42.7}Fe_{9.2}$) increased and the in-plane H_c of the Ni-rich compositions (from $Ni_{51.6}Co_{37.4}Fe_{11}$ to $Ni_{57.1}Co_{30.6}Fe_{12.3}$) decreased. From ML_{300} to ML_{500}, the in-plane H_c of the Co-rich compositions (from $Co_{61.3}Ni_{33.2}Fe_{6.8}$ to $Co_{48.1}Ni_{42.7}Fe_{9.2}$) decreased and the in-plane H_c of the Ni-rich compositions (from $Ni_{47.1}Co_{42.8}Fe_{10.1}$ to $Ni_{57.1}Co_{30.6}Fe_{12.3}$) increased.

The in-plane H_c of Co-rich compositions (from $Co_{61.3}Ni_{33.2}Fe_{6.8}$ to $Co_{48.1}Ni_{42.7}Fe_{9.2}$) of the TFA library $ML_{500\text{-}SC}$ decreased compared to that of the TFA library ML_{RT}. For Ni-rich compositions in this annealed film, the in-plane H_c changed by less than 3 Oe, except for $Ni_{57.1}Co_{30.6}Fe_{12.3}$ where the in-plane H_c increased by 10 Oe, compared to that

Table 2
Morphology, grain size, maximum surface void network length (SVNL), and maximum surface void network width (SVNW) of the TFA libraries.

	Film library	Morphology	Grain size (nm)	Maximum SVNL (nm)	Maximum SVNW (nm)
(a)	MLRT	Particle-like structure with some surface void network formation	69	665.9	37
(b)	ML300	Large granular structure with moderate surface void network formation	98.6	1365	45
(c)	ML500	Uniform, spherical particle structure	63.4	–	–
(e)	ML500-SC	Granular structure with high surface void network formation	82	–	–
(f)	ML700-SC	Non-uniform, equiaxed large particle structure, high density of surface void networks	152.5	–	–

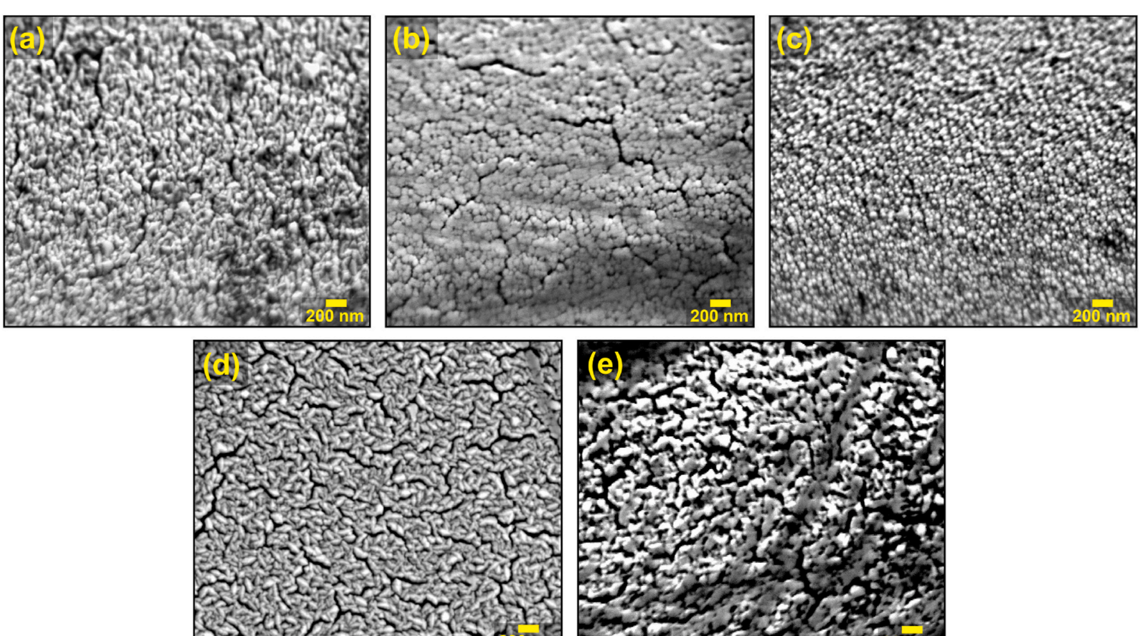

Fig. 4. SEM images of Co-rich section of various Fe-Co-Ni films: (a) ML_{RT}, (b) ML_{300}, (c) ML_{500}, (d) $ML_{500\text{-}SC}$, and (e) $ML_{700\text{-}SC}$.

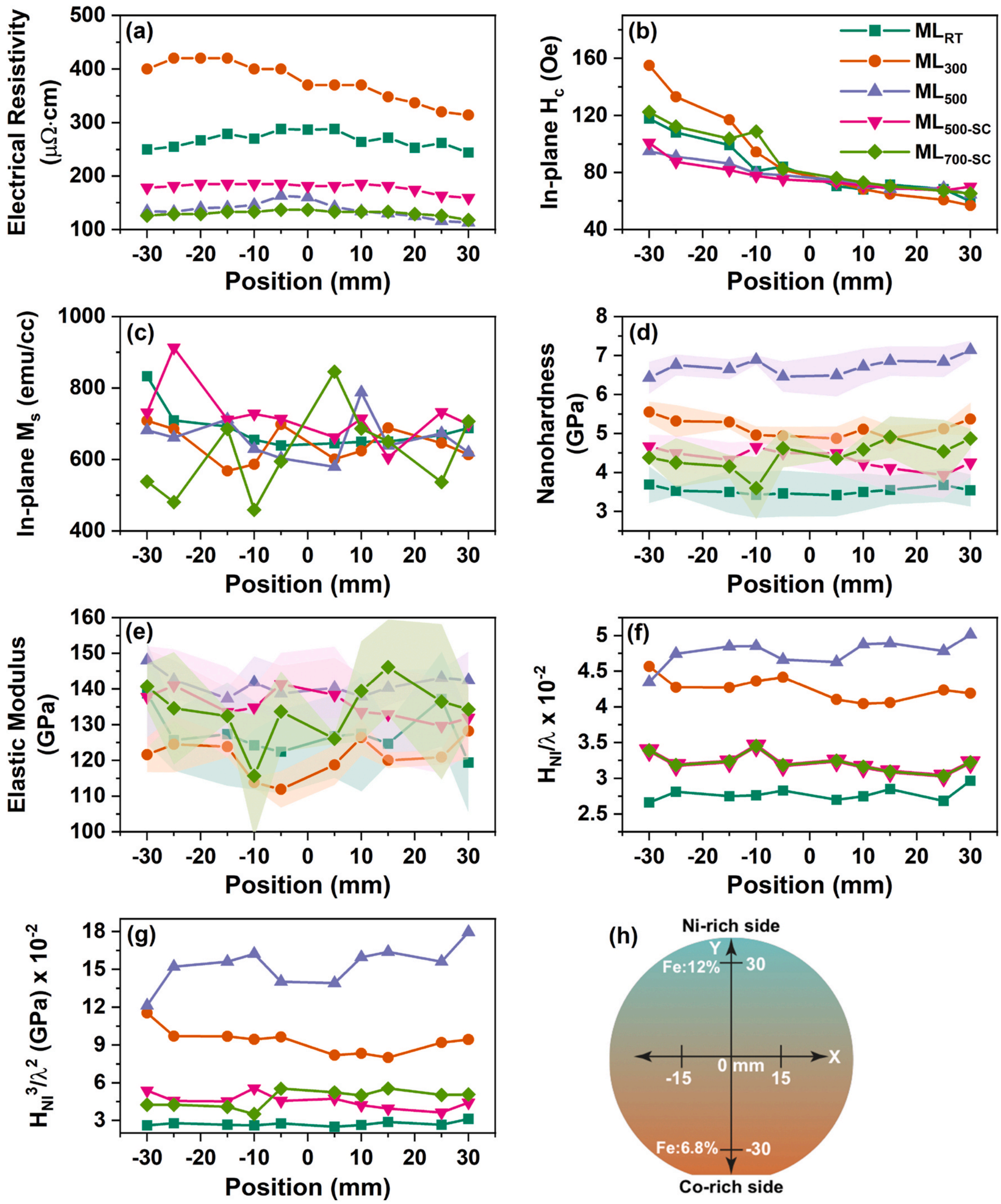

Fig. 5. Property assessment of compositionally graded TFA libraries. (a) Electrical Resistivity, (b) In-plane H_c, (c) In-plane M_s, (d) Nanohardness (H_{NI}), (e) Elastic Modulus (λ), (f) Wear Resistance (H_{NI}/λ), (g) Yield Pressure (H_{NI}^3/λ^2), and (h) Schematic of TFA library for rapid property assessment along x = 0 mm. Notation: Library ML_t where t denotes substrate temperature during deposition and Library $ML_{T\text{-}SC}$ where T denotes annealing temperature after deposition.

of the film ML_{RT}.

The in-plane H_c of the compositions of the TFA library $ML_{700\text{-}SC}$ increased compared to that of the TFA library ML_{RT}, except for $Co_{48.1}Ni_{42.7}Fe_{9.2}$, $Ni_{51.6}Co_{37.4}Fe_{11}$, and $Ni_{55.4}Co_{32.6}Fe_{12}$ wherein the in-plane H_c decreased slightly. Moreover, the in-plane H_c of the compositions of TFA library $ML_{700\text{-}SC}$ was higher compared to that of TFA library $ML_{500\text{-}SC}$, except for $Ni_{55.4}Co_{32.6}Fe_{12}$ and $Ni_{57.1}Co_{30.6}Fe_{12.3}$ wherein it decreased slightly.

Overall, it can be observed that the Co-rich compositions have higher in-plane H_c compared to that of Ni-rich compositions. This can be attributed to the higher magnetocrystalline anisotropy of Co compared to Ni and Fe in the FCC phase [4,41,42]. Additionally, in the HCP phase, due to the combined effect of shape and magnetocrystalline anisotropy, the coercivity tends to be higher [43,44], hence the high coercivity values of high HCP/FCC volume ratio compositions compared to low HCP/FCC volume ratios.

The in-plane M_s of the TFA library ML_{RT} initially decreased from 833 to 639 emu/cc with decreasing Co content until the $Co_{48.1}Ni_{42.7}Fe_{9.2}$ compositions, where the Co and Ni content are almost equal, and then increased from 645 to 688 emu/cc with increasing Ni content. For ML_{300}, the in-plane M_s varied in the range from 568 to 708.3 emu/cc. For ML_{500}, the in-plane M_s varied in the range from 579.4 to 787.8 emu/

cc. For $ML_{500\text{-}SC}$, the in-plane M_s varied in the range from 605.4 to 912.6 emu/cc. For $ML_{700\text{-}SC}$, the in-plane M_s varied in the range from 459.2 to 845.6 emu/cc. The out-of-plane H_c and M_s of the TFA libraries are discussed in the section S2 of supplementary information.

3.7. Mechanical properties of the film libraries

3.7.1. Nano hardness

The nanohardness of the TFA libraries ML_{RT}, ML_{300}, and ML_{500} (Fig. 5(d)), increased with higher T_s due to the better crystallinity, as mentioned before. The nanohardness varied in the range 3.42 ± 0.54–3.69 ± 0.47 GPa, for ML_{RT}, 4.87 ± 0.33–5.55 ± 0.27 GPa for ML_{300}, and 6.43 ± 0.41–7.14 ± 0.24 GPa for ML_{500}. For the TFA libraries ML_{RT} and ML_{300}, the $Co_{61.3}Ni_{33.2}Fe_{6.8}$ composition exhibited the highest nanohardness. However, in ML_{500}, this composition exhibited the lowest nanohardness. $Ni_{47.1}Co_{42.8}Fe_{10.1}$ exhibited the lowest nanohardness for the TFA libraries ML_{RT} and ML_{300} and a low nanohardness value for ML_{500}. The nanohardness of TFA libraries $ML_{500\text{-}SC}$ and $ML_{700\text{-}SC}$ (Fig. 5 (d)) are higher compared to that of the TFA library ML_{RT}. The nanohardness varied in the range 3.93 ± 0.59–4.67 ± 0.3 GPa for $ML_{500\text{-}SC}$ and 3.6 ± 0.8–4.91 ± 0.53 GPa for $ML_{700\text{-}SC}$.

After annealing, the nanohardness of ML_{RT} increased due to the transformation of the amorphous phase to the crystalline phase [45]. With an increase in annealing temperature from 500 °C to 700 °C, the nanohardness decreased for the composition range ($Co_{61.3}Ni_{33.2}Fe_{6.8}$ to $Ni_{47.1}Co_{42.8}Fe_{10.1}$) which exhibited a two-phase HCP and FCC structure. This can be attributed to the increase in the HCP phase volume fraction for higher annealing temperature. An exception was $Co_{48.1}Ni_{42.7}Fe_{9.2}$ which showed increased nanohardness, from 4.5 ± 0.32 GPa to 4.62 ± 0.49 GPa. For the composition range $Ni_{53.7}Co_{34.8}Fe_{11.5}$ to $Ni_{57.1}Co_{30.6}Fe_{12.3}$, with an increase in annealing temperature from 500 °C to 700 °C, the nanohardness also became larger. These compositions exhibited the FCC phase and higher crystallinity at larger annealing temperatures.

In the TFA library $ML_{500\text{-}SC}$, the compositions consisting of a single FCC phase show lower nanohardness compared to those compositions which consist of a two-phase HCP and FCC structure. However, in the TFA library $ML_{700\text{-}SC}$, the composition consisting of single FCC phase show higher hardness compared to the compositions consisting of mixed HCP and FCC phase structure.

3.7.2. Elastic modulus

The elastic modulus of the TFA libraries ML_{RT}, ML_{300}, and ML_{500} (Fig. 5(e)) initially decreased with a change in T_s from RT to 300 °C and then increased with a further change in T_s from 300 °C to 500 °C. The only exception is for $Ni_{57.1}Co_{30.6}Fe_{12.3}$, whose elastic modulus increases from 119.41 ± 13.92 GPa to 128.21 ± 7.87 GPa and further to 142.44 ± 8.01 GPa with increasing T_s from RT to 300 °C and further to 500 °C, respectively. The elastic modulus varied in the range 119.41 ± 13.92–138.72 ± 14.11 GPa for ML_{RT}, 111.91 ± 5.1–128.21 ± 7.87 GPa for ML_{300}, and 137.3 ± 3.03–147.98 ± 2.99 GPa for ML_{500}. The elastic modulus of the TFA library $ML_{500\text{-}SC}$ increased compared to that of ML_{RT}, except for $Co_{61.3}Ni_{33.2}Fe_{6.8}$ and $Ni_{55.4}Co_{32.6}Fe_{12}$. The elastic modulus of the TFA library $ML_{700\text{-}SC}$ increased for $Co_{61.3}Ni_{33.2}Fe_{6.8}$, decreased for lower Co content until $Ni_{47.1}Co_{42.8}Fe_{10.1}$, and finally increased for higher Ni content compared to that of $ML_{500\text{-}SC}$

The compositions for which elastic modulus decreased with higher annealing temperature exhibit a two-phase structure. This change may be attributed to a change in texture or an ordering transformation at high temperatures [21,46]. There is no significant change in elastic modulus values with change in composition in a single TFA library. However, the elastic modulus of a given composition does vary with a change in substrate temperature and annealing temperature.

3.7.3. Wear resistance and yield pressure

Apart from nanohardness and elastic modulus, nanoindentation can be used to determine other parameters related to the service life [21, 47–49]. A material with higher hardness can exhibit better wear resistance [50]. The ratio of nanohardness and elastic modulus (H_{NI}/λ), which describes the material's ability to resist elastic strain to failure, is also related to the wear resistance of the material [21,47,48]. A parameter, H_{NI}^3/λ^2 (known as yield pressure), indicates the material's ability to resist plastic deformation [48,49]. Fig. 5(f) and (g) displays the H_{NI}/λ and H_{NI}^3/λ^2 of the various TFA libraries. For higher T_s, both these ratios increased, indicating better wear resistance and plastic deformation resistance. The only exception is the decrease of H_{NI}/λ for $Co_{61.3}Ni_{33.2}Fe_{6.8}$ with an increase in T_s from 300 °C to 500 °C. The ratio H_{NI}/λ increased upon annealing of the TFA libraries but does not change significantly at higher annealing temperature.

The ratio H_{NI}^3/λ^2 increased for the TFA library $ML_{500\text{-}SC}$ compared to the TFA library ML_{RT}. However, on increasing the annealing temperature from 500 °C to 700 °C, H_{NI}^3/λ^2 decreased in the composition range $Co_{61.3}Ni_{33.2}Fe_{6.8}$ to $Co_{50.6}Ni_{40.7}Fe_{8.7}$ and then increased for the composition range $Co_{48.1}Ni_{42.7}Fe_{9.2}$ to $Ni_{57.1}Co_{30.6}Fe_{12.3}$. The highest H_{NI}/λ and H_{NI}^3/λ^2 is observed for $Ni_{57.1}Co_{30.6}Fe_{12.3}$ of the TFA library ML_{500}.

3.8. Consolidated property set

Selected results are summarized in Fig. 6. Fig. 6(a) shows a donut heatmap of several properties, including electrical resistivity (ρ), in-plane M_s, H_c, nanohardness (H_{NI}), elastic modulus (λ), H_{NI}/λ, H_{NI}^3/λ^2, and cost of the TFA library ML_{500}. The properties are min-max scaled between 0 and 1. Among the five material libraries, the TFA library ML_{500} exhibited highest crystallinity, the most uniform surface morphology, highest values of mechanical and wear resistance properties (including H_{NI}, λ, H_{NI}/λ, and H_{NI}^3/λ^2), lowest in-plane H_c values, and moderate ρ values. Fig. 6(b) shows the variation of various properties with composition of the ML_{500} film library stacked along the y-axis. The property values in this plot are not normalized, unlike the donut heatmap.

The $Ni_{54.9}Co_{33.1}Fe_{12}$ composition exhibited the highest values of hardness, wear resistance, yield pressure; lowest values of H_c, cost, ρ; and moderate values of λ and M_s. The electrical resistivity (113 μΩ cm) is higher than the values of permalloy thin films (57 μΩ cm for 15 nm thin films and 31 μΩ cm for 30 nm thin films) [51] and similar to the corresponding values for permalloy thin films with the addition of V, Mo, and W (103 μΩ cm for $Ni_{83}Fe_{10}V_7$, 128 μΩ cm for $Ni_{83.5}Fe_{7.6}Mo_{8.9}$, 145 μΩ cm for $Ni_{83.5}Fe_{7.6}W_{8.9}$) [52]. Thus, we have identified a composition with an attractive combination of properties: moderate to high M_s, ρ, λ; low H_c; high H_{NI}, wear resistance, and yield pressure, which makes *this composition a promising candidate for applications in electrical machines.*

$Ni_{53}Co_{35.4}Fe_{11.6}$ is another promising composition with low values of H_c and cost and moderate values of M_s, mechanical properties, and ρ.

The Co rich composition $Co_{59.7}Ni_{33.2}Fe_{7.2}$ shows moderate values of mechanical properties, M_s, and high values of H_c and ρ which can be useful. e.g., as a semi-hard magnetic material for magnetic recording media [53], electronic article surveillance devices [54], hysteresis motor [55], or magnetorheological actuator [56]. A drawback is the high cost.

Thus, new alloy compositions with the desired combination of properties could be identified by combinatorial co-sputtering of materials libraries spanning a broad ternary composition space and various process parameters.

4. Conclusions

A combinatorial synthesis of compositionally graded Fe-Co-Ni TFA libraries processed by magnetron co-sputtering was conducted. Their structural, magnetic (in-plane M_s and H_c), electrical (ρ), and mechanical properties (H_{NI}, λ, H_{NI}/λ , H_{NI}^3/λ^2) were rapidly evaluated.

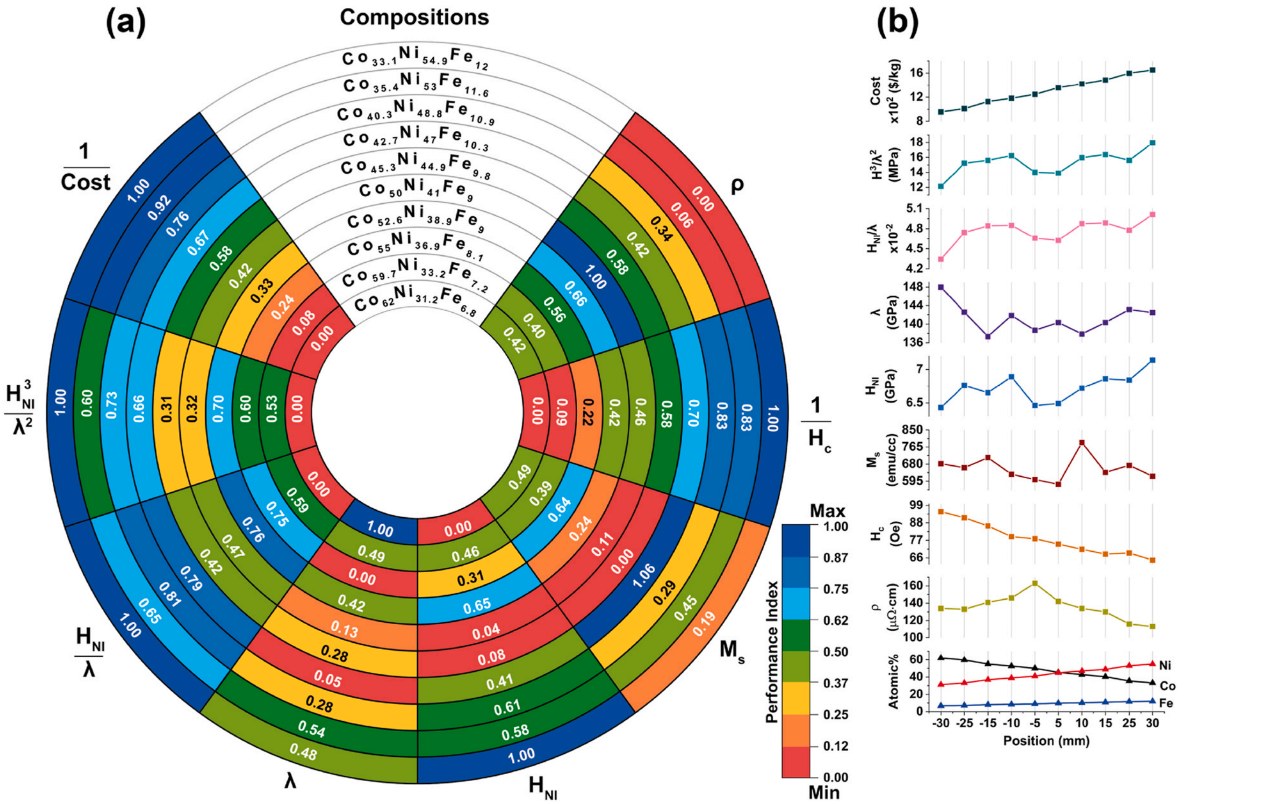

Fig. 6. Consolidated composition and properties of ML_{500} TFA library. (a) Donut heatmap (0 – minimum and 1 – maximum) and (b) stacked y-axis plot. Notation: electrical resistivity (ρ), coercivity (H_C), saturation magnetization (M_S), nanohardness (H_{NI}), elastic modulus (λ), wear resistance (H_{NI}/λ), yield pressure (H_{NI}^3/λ^2).

- A significant variation in H_c with a change in composition and processing temperature was observed. ρ varied significantly with a change in processing temperature. H_{NI} and λ varied substantially with a change in substrate temperature.
- The Fe-Co-Ni TFA library sputtered at $T_s = 500$ °C showed a good combination of magnetic, mechanical, and electrical properties. $Ni_{54.9}Co_{33.1}Fe_{12}$ exhibited high values of H_{NI}, H_{NI}/λ , H_{NI}^3/λ^2, lower values of H_c and moderate values of ρ, M_s, λ, which can be suitable for high wear resistance and strength applications such as high frequency transformers, electric motors and inductors used in extreme service conditions.
- $Co_{59.7}Ni_{33.2}Fe_{7.2}$ exhibited moderate values of M_s, λ, H_{NI}, H_{NI}/λ , H_{NI}^3/λ^2, H_c, and ρ, which can be suitable for disc drive, hysteresis motor, and actuator applications. Thus, combinatorial TFA libraries can be developed for rapid assessment of structural, magnetic, mechanical, and electrical properties over a broad composition and process parameter space.

Declaration of competing interest

The authors declare that they have no known competing financial interests or personal relationships that could have appeared to influence the work reported in this paper.

Acknowledgement

This work is supported by the AME Programmatic Fund by the Agency for Science, Technology and Research, Singapore under Grant No. A1898b0043. We would like to acknowledge the Facility for Analysis, Characterization, Testing and Simulation, Nanyang Technological University, Singapore, for use of their electron microscopy, EPMA, X-ray facilities. We thank Dr. Vijaykumar B. Varma for his assistance in figures and data visualization and for comments on the manuscript.

Appendix A. Supplementary data

Supplementary data to this article can be found online at https://doi.org/10.1016/j.rinma.2022.100283.

References

[1] K.M. Krishnan, Fundamentals and Applications of Magnetic Materials, Oxford University Press, 2016, https://doi.org/10.1093/acprof:oso/9780199570447.001.0001.
[2] V. Chaudhary, S.A. Mantri, R.V. Ramanujan, R. Banerjee, Additive manufacturing of magnetic materials, Prog. Mater. Sci. 114 (2020) 100688, https://doi.org/10.1016/j.pmatsci.2020.100688.
[3] O. Gutfleisch, M.A. Willard, E. Brück, C.H. Chen, S. Sankar, J.P. Liu, Magnetic materials and devices for the 21st century: stronger, lighter, and more energy efficient, Adv. Mater. 23 (2011) 821–842, https://doi.org/10.1002/adma.201002180, doi:.
[4] V. Chaudhary, L.P. Tan, V.K. Sharma, R. Ramanujan, Accelerated study of magnetic Fe-Co-Ni alloys through compositionally graded spark plasma sintered samples, J. Alloys Compd. 869 (2021) 159318, https://doi.org/10.1016/j.jallcom.2021.159318.
[5] V. Raposo, M. Zazo, A. Flores, J. Garcia, V. Vega, J. Iñiguez, V. Prida, Ferromagnetic resonance in low interacting permalloy nanowire arrays, J. Appl. Phys. 119 (2016) 143903, https://doi.org/10.1063/1.4945762.
[6] M.R.J. Gibbs, E.W. Hill, P.J. Wright, Magnetic materials for MEMS applications, J. Phys. D Appl. Phys. 37 (2004) R237–R244, https://doi.org/10.1088/0022-3727/37/22/R01, doi:.
[7] D. Moreels, P. Leijnen, Turning the electric motor inside out: a Belgian startup's axial-flux motor for EVs is small, light, and powerful, IEEE Spectrum 56 (2019) 40–45.
[8] M.E. McHenry, D.E. Laughlin, Magnetic properties of metals and alloys, in: Physical Metallurgy, Elsevier, 2014, pp. 1881–2008.
[9] Y. Iwasaki, R. Sawada, E. Saitoh, M. Ishida, Machine learning autonomous identification of magnetic alloys beyond the Slater-Pauling limit, Commun. Mater. 2 (2021) 1–7, https://doi.org/10.1038/s43246-021-00135-0, doi:.
[10] C. Mikler, V. Chaudhary, T. Borkar, V. Soni, D. Choudhuri, R. Ramanujan, R. Banerjee, Laser additive processing of Ni-Fe-V and Ni-Fe-Mo permalloys: microstructure and magnetic properties, Mater. Lett. 192 (2017) 9–11, https://doi.org/10.1016/j.matlet.2017.01.059, doi:.
[11] G. Ouyang, X. Chen, Y. Liang, C. Macziewski, J. Cui, Review of Fe-6.5 wt% Si high silicon steel—a promising soft magnetic material for sub-kHz application, J. Magn.

Magn Mater. 481 (2019) 234–250, https://doi.org/10.1016/j.jmmm.2019.02.089, doi:.

[12] T.N. Lamichhane, L. Sethuraman, A. Dalagan, H. Wang, J. Keller, M. P. Paranthaman, Additive manufacturing of soft magnets for electrical machines—a review, Mater. Today Phys. (2020) 100255, https://doi.org/10.1016/j.mtphys.2020.100255.

[13] V. Chaudhary, N.M.S.K.K. Yadav, S.A. Mantri, S. Dasari, A. Jagetia, R. Ramanujan, R. Banerjee, Additive manufacturing of functionally graded Co–Fe and Ni–Fe magnetic materials, J. Alloys Compd. 823 (2020) 153817, https://doi.org/10.1016/j.jallcom.2020.153817.

[14] S.W. Fackler, V. Alexandrakis, D. König, A.G. Kusne, T. Gao, M.J. Kramer, D. Stasak, K. Lopez, B. Zayac, A. Mehta, Combinatorial study of Fe-Co-V hard magnetic thin films, Sci. Technol. Adv. Mater. 18 (2017) 231–238, https://doi.org/10.1080/14686996.2017.1287520, doi:.

[15] L. Han, Z. Rao, I.R. Souza Filho, F. Maccari, Y. Wei, G. Wu, A. Ahmadian, X. Zhou, O. Gutfleisch, D. Ponge, D. Raabe, Z. Li, Ultrastrong and ductile soft magnetic high-entropy alloys via coherent ordered nanoprecipitates, Adv. Mater. 33 (2021) 2102139, https://doi.org/10.1002/adma.202102139.

[16] S.S. Mao, P.E. Burrows, Combinatorial screening of thin film materials: an overview, J. Materiomics 1 (2015) 85–91, https://doi.org/10.1016/j.jmat.2015.04.002, doi:.

[17] L. Himanen, A. Geurts, A.S. Foster, P. Rinke, Data-driven materials science: status, challenges, and perspectives, Adv. Sci. 6 (2019) 1900808, https://doi.org/10.1002/advs.201900808.

[18] M.L. Green, I. Takeuchi, J.R. Hattrick-Simpers, Applications of high throughput (combinatorial) methodologies to electronic, magnetic, optical, and energy-related materials, J. Appl. Phys. 113 (2013) 9_1, https://doi.org/10.1063/1.4803530.

[19] H. Xing, B. Zhao, Y. Wang, X. Zhang, Y. Ren, N. Yan, T. Gao, J. Li, L. Zhang, H. Wang, Rapid construction of Fe-Co-Ni composition-phase map by combinatorial materials chip approach, ACS Comb. Sci. 20 (2018) 127–131, https://doi.org/10.1021/acscombsci.7b00171, doi:.

[20] A. Ludwig, Discovery of new materials using combinatorial synthesis and high-throughput characterization of thin-film materials libraries combined with computational methods, Npj Comput. Mater. 5 (2019) 1–7, https://doi.org/10.1038/s41524-019-0205-0, doi:.

[21] V. Chaudhary, R. Chaudhary, R. Banerjee, R.V. Ramanujan, Accelerated and conventional development of magnetic high entropy alloys, Mater. Today 49 (2021) 231–252, https://doi.org/10.1016/j.mattod.2021.03.018, doi:.

[22] T. Borkar, R. Conteri, X. Chen, R. Ramanujan, R. Banerjee, Laser additive processing of functionally-graded Fe–Si–B–Cu–Nb soft magnetic materials, Mater. Manuf. Process. 32 (2017) 1581–1587, https://doi.org/10.1080/10426914.2016.1244849, doi:.

[23] M. Li, J. Gazquez, A. Borisevich, R. Mishra, K.M. Flores, Evaluation of microstructure and mechanical property variations in AlxCoCrFeNi high entropy alloys produced by a high-throughput laser deposition method, Intermetallics 95 (2018) 110–118, https://doi.org/10.1016/j.intermet.2018.01.021.

[24] P. Decker, D. Naujoks, D. Langenkämper, C. Somsen, A. Ludwig, High-throughput structural and functional characterization of the thin film materials system Ni–Co–Al, ACS Comb. Sci. 19 (2017) 618–624, https://doi.org/10.1021/acscombsci.6b00176, doi:.

[25] J.R. Hattrick-Simpers, A. Zakutayev, S.C. Barron, Z.T. Trautt, N. Nguyen, K. Choudhary, B. DeCost, C. Phillips, A.G. Kusne, F. Yi, An inter-laboratory study of Zn–Sn–Ti–O thin films using high-throughput experimental methods, ACS Comb. Sci. 21 (2019) 350–361, https://doi.org/10.1021/acscombsci.8b00158, doi:.

[26] S. Burger, C. Eberl, A. Siegel, A. Ludwig, O. Kraft, A novel high-throughput fatigue testing method for metallic thin films, Sci. Technol. Adv. Mater. 12 (2011), 054202, https://doi.org/10.1088/1468-6996/12/5/054202.

[27] V. Alexandrakis, W. Wallisch, S. Hamann, G. Varvaro, J. Fidler, A. Ludwig, Combinatorial development of Fe–Co–Nb thin film magnetic nanocomposites, ACS Comb. Sci. 17 (2015) 698–703, https://doi.org/10.1021/acscombsci.5b00116, doi:.

[28] J. Cui, Y.S. Chu, O.O. Famodu, Y. Furuya, J. Hattrick-Simpers, R.D. James, A. Ludwig, S. Thienhaus, M. Wuttig, Z. Zhang, Combinatorial search of thermoelastic shape-memory alloys with extremely small hysteresis width, Nat. Mater. 5 (2006) 286–290, https://doi.org/10.1038/nmat1593, doi:.

[29] N.M. Al Hasan, H. Hou, T. Gao, J. Counsell, S. Sarker, S. Thienhaus, E. Walton, P. Decker, A. Mehta, A. Ludwig, Combinatorial exploration and mapping of phase transformation in a Ni–Ti–Co thin film library, ACS Comb. Sci. 22 (2020) 641–648, https://doi.org/10.1021/acscombsci.0c00097, doi:.

[30] T.A. Aljohani, B.E. Hayden, A. Anastasopoulos, The high throughput electrochemical screening of the corrosion resistance of Ni–Cr thin film alloys, Electrochim. Acta 76 (2012) 389–393, https://doi.org/10.1016/j.electacta.2012.05.045, doi:.

[31] Y.K. Yoo, T. Ohnishi, G. Wang, F. Duewer, X.-D. Xiang, Y.S. Chu, D.C. Mancini, Y.-Q. Li, R.C. O'Handley, Continuous mapping of structure–property relations in Fe1−xNix metallic alloys fabricated by combinatorial synthesis, Intermetallics 9 (2001) 541–545, https://doi.org/10.1016/S0966-9795(01)00030-9.

[32] Y.K. Yoo, Q. Xue, Y.S. Chu, S. Xu, U. Hangen, H.-C. Lee, W. Stein, X.-D. Xiang, Identification of amorphous phases in the Fe–Ni–Co ternary alloy system using continuous phase diagram material chips, Intermetallics 14 (2006) 241–247, https://doi.org/10.1016/j.intermet.2005.05.013.

[33] M. Kumar, Effect of substrate temperature on surface morphology and optical properties of sputter deposited nanocrystalline nickel oxide films, Mater. Res. Express 6 (2019), 096404, https://doi.org/10.1088/2053-1591/ab2af2.

[34] E. Kusano, Structure-zone modeling of sputter-deposited thin films: a brief review, Appl. Sci. Converg. Technol. 28 (2019) 179–185, https://doi.org/10.5757/ASCT.2019.28.6.179, doi:.

[35] T.M. Donovan, K. Heinemann, High-resolution electron microscope observation of voids in amorphous Ge, Phys. Rev. Lett. 27 (1971) 1794–1796, https://doi.org/10.1103/PhysRevLett.27.1794.

[36] C.-H. Tsau, Z.-Y. Hwang, S.-K. Chen, The microstructures and electrical resistivity of (Al, Cr, Ti) FeCoNiOx high-entropy alloy oxide thin films, Adv. Mater. Sci. Eng. 2015 (2015) 1–6, https://doi.org/10.1155/2015/353140.

[37] I. Bakonyi, V. Isnaini, T. Kolonits, Z. Czigány, J. Gubicza, L. Varga, E. Tóth-Kádár, L. Pogány, L. Péter, H. Ebert, The specific grain-boundary electrical resistivity of Ni, Philos. Mag. A 99 (2019) 1139–1162, https://doi.org/10.1080/14786435.2019.1580399, doi:.

[38] M. Aus, B. Szpunar, U. Erb, A. El-Sherik, G. Palumbo, K. Aust, Electrical resistivity of bulk nanocrystalline nickel, J. Appl. Phys. 75 (1994) 3632–3634, https://doi.org/10.1063/1.356076, doi:.

[39] Y.J. Kim, S.-G. Kang, Y. Oh, G.W. Kim, I.H. Cha, H.N. Han, Y.K. Kim, Microstructural evolution and electrical resistivity of nanocrystalline W thin films grown by sputtering, Mater. Char. 145 (2018) 473–478, https://doi.org/10.1016/j.matchar.2018.09.016, doi:.

[40] Y. Zhang, T. Zuo, Y. Cheng, P.K. Liaw, High-entropy alloys with high saturation magnetization, electrical resistivity and malleability, Sci. Rep. 3 (2013) 1–7, https://doi.org/10.1038/srep01455.

[41] A. Leary, V. Keylin, A. Devaraj, V. DeGeorge, P. Ohodnicki, M.E. McHenry, Stress induced anisotropy in Co-rich magnetic nanocomposites for inductive applications, J. Mater. Res. 31 (2016) 3089–3107, https://doi.org/10.1557/jmr.2016.324, doi:.

[42] M. Cheng, M. Wen, S. Zhou, Q. Wu, B. Sun, Solvothermal synthesis of NiCo alloy icosahedral nanocrystals, Inorg. Chem. 51 (2012) 1495–1500, https://doi.org/10.1021/ic201763j.

[43] H. Sato, O. Kitakami, T. Sakurai, Y. Shimada, Y. Otani, K. Fukamichi, Structure and magnetism of hcp-Co fine particles, J. Appl. Phys. 81 (1997) 1858–1862, https://doi.org/10.1063/1.364041.

[44] L.G. Vivas, M. Vazquez, J. Escrig, S. Allende, D. Altbir, D.C. Leitao, J.P. Araujo, Magnetic anisotropy in CoNi nanowire arrays: analytical calculations and experiments, Phys. Rev. B 85 (2012), 035439, https://doi.org/10.1103/PhysRevB.85.035439.

[45] P. Nayar, A. Khanna, D. Kabiraj, S.R. Abhilash, B.D. Beake, Y. Losset, B. Chen, Structural, optical and mechanical properties of amorphous and crystalline alumina thin films, Thin Solid Films 568 (2014) 19–24, https://doi.org/10.1016/j.tsf.2014.07.053.

[46] S. Hasani, M. Shamanian, A. Shafyei, M. Nezakat, H. Mostaan, J.A. Szpunar, Effect of recrystallization and phase transitions on the mechanical properties of semihard magnetic FeCo-7.15 V alloy during the thermomechanical process, Metall. Mater. Trans. 48 (2017) 1903–1909, https://doi.org/10.1007/s11661-017-3954-8, doi:.

[47] H. Attar, S. Ehtemam-Haghighi, D. Kent, I. Okulov, H. Wendrock, M. Bönisch, A. Volegov, M. Calin, J. Eckert, M. Dargusch, Nanoindentation and wear properties of Ti and Ti-TiB composite materials produced by selective laser melting, Mater. Sci. Eng., A 688 (2017) 20–26, https://doi.org/10.1016/j.msea.2017.01.096, doi:.

[48] S. Ehtemam-Haghighi, G. Cao, L.-C. Zhang, Nanoindentation study of mechanical properties of Ti based alloys with Fe and Ta additions, J. Alloys Compd. 692 (2017) 892–897, https://doi.org/10.1016/j.jallcom.2016.09.123, doi:.

[49] J. Fornell, N. Van Steenberge, A. Varea, E. Rossinyol, E. Pellicer, S. Suriñach, M. Baró, J. Sort, Enhanced mechanical properties and in vitro corrosion behavior of amorphous and devitrified Ti40Zr10Cu38Pd12 metallic glass, J. Mech. Behav. Biomed. Mater. 4 (2011) 1709–1717, https://doi.org/10.1016/j.jmbbm.2011.05.028, doi:.

[50] J. Xu, G. dong Wang, X. Lu, L. Liu, P. Munroe, Z.-H. Xie, Mechanical and corrosion-resistant properties of Ti–Nb–Si–N nanocomposite films prepared by a double glow discharge plasma technique, Ceram. Int. 40 (2014) 8621–8630, https://doi.org/10.1016/j.ceramint.2014.01.079.

[51] I. Pazukha, O.V. Pylypenko, L. Odnodvorets, A comprehensive investigation of electrophysical and magnetoresistive properties of thin films based on permalloy and silver, Mater. Res. Express 5 (2018) 106409, https://doi.org/10.1088/2053-1591/aadb54.

[52] M. Banerjee, A. Majumdar, A. Nigam, Electron transport in permalloys with V/Mo/W additions, Phys. B Condens. Matter 431 (2013) 84–88, https://doi.org/10.1016/j.physb.2013.08.032, doi:.

[53] P.C. Andricacos, N. Robertson, Future directions in electroplated materials for thin-film recording heads, IBM J. Res. Dev. 42 (1998) 671–680, https://doi.org/10.1147/rd.425.0671, doi:.

[54] G. Herzer, Magnetic materials for electronic article surveillance, J. Magn. Magn Mater. 254–255 (2003) 598–602, https://doi.org/10.1016/S0304-8853(02)00930-7, doi:.

[55] M.M. Firozjaee, A. Vahedi, M. Sanikhani, Comparing the effect of using new hysteresis material on the performance of a hystersis motor, in: 7th Power Electronics and Drive Systems Technologies Conference, PEDSTC), 2016, pp. 24–28, 2016.

[56] A. Wiehe, J. Maas, Magnetorheological actuators with currentless bias torque for automotive applications, J. Intell. Mater. Syst. Struct. 21 (2010) 1575–1585, https://doi.org/10.1177/1045389X10385487.